Journal of Hydrology 377 (2009) 120–130

Contents lists available at ScienceDirect

Journal of Hydrology

journal homepage: www.elsevier.com/locate/jhydrol

Calibration of a groundwater model using pattern information from remote sensing data

H.T. Li [a,*], P. Brunner [b], W. Kinzelbach [a], W.P. Li [c], X.G. Dong [d]

[a] Institute of Environmental Engineering (IfU), ETH Zurich, CH-8093, Switzerland
[b] School of Chemistry, Physics and Earth Sciences, Flinders University, 5001, Australia
[c] China Institute of Geo-Environmental Monitoring, Beijing 100081, China
[d] Xinjiang Agricultural University, Urumqi 830052, China

ARTICLE INFO

Article history:
Received 10 November 2008
Received in revised form 24 June 2009
Accepted 7 August 2009

This manuscript was handled by P. Baveye.

Keywords:
Groundwater modeling
Model calibration
Phreatic evaporation
Remote sensing
Pattern information

SUMMARY

Due to the chronic lack of verification data, hydrologic models are notoriously over-parameterized. If a large number of parameters are estimated, while few verification data are available, the calibrated model may have little predictive value. However, recent development in remote sensing (RS) techniques allows generation of spatially distributed data that can be used to construct and verify hydrological models. These additional data reduce the ambiguity of the calibration process and thus increase the predictive value of the model. An example for such remotely sensed data is the spatial distribution of phreatic evaporation. In this modeling approach, we use the spatial distribution of phreatic evaporation obtained by remote sensing images as verification data. Compared to the usual limited amount of head data, the spatial distribution of evaporation data provides a complete areal coverage.

However, the absolute values of the evaporation data are uncertain and therefore three ways of using the spatial distribution pattern of evaporation were tested and compared. The first way is to directly use the evaporation pattern defined in a relative manner by dividing the evaporation rate in a pixel by the total evaporation of a selected rectangular area of interest. Alternatively, the discrete fourier transform (DFT) or the discrete wavelet transform (DWT) are applied to the relative evaporation pattern in the space domain defined before. Seven different combinations of using hydraulic head data and/or evaporation pattern data as conditioning information have been tested. The code PEST, based on the least-squares method, was used as an automatic calibration tool.

From the calibration results, we can conclude that the evaporation pattern can replace the head data in the model calibration process, independently of the way the evaporation pattern is introduced into the calibration procedure.

Introduction

Model calibration is a necessary and critical step in groundwater modeling. It is usually carried out by comparing simulated to observed hydraulic heads at a limited number of observation points. In order to achieve a good fit between the observed and simulated values, a number of adjustable parameters are varied in order to minimize the residual between observed and simulated heads by means of a trial and error process (Poeter and Hill, 1997; Gupta et al., 1998). However, if the number of adjustable parameters is large compared to the amount of available observation data, this approach does not yield useful results. Calibrating too many adjustable parameters in comparison to limited observation data allows a perfect fit to data, but results in an over-parameterized groundwater model with little or no predictive value.

Remote sensing (RS) data contain information that can help in setting up and verifying a groundwater model. By interpreting RS images, we can get spatially exhaustive although non-exact verification data in contrast to the traditional limited number of more exact point data. RS data are especially valuable in arid or semi-arid regions where the observation infrastructure is poor. Some successful examples of RS data applications in groundwater modeling can be found in Anon (1990), Bobba et al. (1992), Brunner et al. (2004), Brunner et al. (2007), Choudhury (1994), Du and Ye (1993); El Hadanai et al. (1993), Kite and Pietroniro (1996), Meijerink (1996), and Hendricks Franssen et al. (2008). The spatial distribution of evapotranspiration (ET) is a set of verification data for models which simulate evaporation and transpiration. ET can be calculated from RS images based on the theory of surface energy balance (Hall et al., 1992; Bastiaanssen

* Corresponding author. Address: IfU, ETH Zurich, CH-8093, Switzerland. Tel.: +41 44 633 3082; fax: +41 44 633 1061.
E-mail address: li@ifu.baug.ethz.ch (H.T. Li).

0022-1694/$ - see front matter © 2009 Elsevier B.V. All rights reserved.
doi:10.1016/j.jhydrol.2009.08.012

et al., 1998a,b; Roerink et al., 2000). A comparison between the ET from RS data, hydrological modeling and field data has been carried out by Kite and Droogers (2000). An application of ET data from RS in model calibration has been illustrated by Immerzeel and Droogers, 2007 for a hydrological model established with the Soil and Water Assessment Tool (SWAT) (Arnold et al., 1998).

In groundwater modeling, evaporation and transpiration are usually lumped together as ET and simulated in one term that increases with rising water tables, e.g. the ET-module in MODFLOW (McDonald and Harbaugh, 1988; McDonald and Harbaugh, 1996; Harbaugh et al., 2000). However, in some cases this may not be appropriate, as transpiration depends on more parameters than just the depth to groundwater. More sophisticated ways to treat both terms are presented in Maddock and Baird (2003) for the riparian environment, Schmid et al. (2006) for irrigated areas and Bauer et al. (2006) for a natural environment.

In this study, we concentrate on evaporation instead of ET. The spatial distribution pattern of evaporation data from the RS images was taken as conditioning information in the model calibration process. Instead of using the absolute values of evaporation rates, the relative spatial distribution pattern has been studied. This approach acknowledges that uncertainty exists in the absolute evaporation rates from RS data (see also Brunner et al., 2007; Hendricks Franssen et al., 2008). We will discuss the results obtained from calibration using three different ways of introducing the spatial distribution pattern into the calibration procedure. Also, the use of different combinations of hydraulic head data and evaporation pattern data from RS images in the calibration procedure will be discussed. PEST (Doherty, 2005) is used throughout as an automatic model calibration tool.

Characterizations of the spatial distribution pattern

The pattern of an image can be characterized in the spatial domain or the frequency domain. In this paper, we (1) use a pattern defined on the basis of relative values in the spatial domain, and characterize it in the frequency domain by (2) a discrete fourier transformation (DFT) and (3) a discrete wavelet transform (DWT). The patterns are used individually in the automatic calibration procedure, defining a squared "distance" between the computed evaporation pattern and the observed evaporation pattern as a goal function which is to be minimized. The "distance" can be the sum of the pixel by pixel squared differences between computed and observed images in the spatial domain or the squared differences of the values obtained after applying DFT or DWT to both computation results and RS data.

Characterization of a pattern by relative values in the spatial domain

Each pixel value is divided by the sum of the pixel values over the entire image. This image represents the relative values which are of interest, as the relative pattern information is more reliable than the absolute values which are obtained from the RS data.

Characterization of pattern by discrete fourier transformation (DFT)

The discrete fourier transformation is a useful and important image processing tool. The result of the transformation is the representation of the image in the frequency domain while the original image is shown in the spatial domain. For the image represented in the frequency domain, each matrix element value is associated with a particular frequency contained in the spatial domain image. For digital image processing the DFT is often applied. A detailed explanation of the DFT procedure is given by e.g. Pratt (2001).

The mathematical formulation of a two dimensional DFT to a digital image with a size of M rows by N columns is given by:

$$F(u,v) = \frac{1}{\sqrt{M \cdot N}} \sum_{j=0}^{M-1} \sum_{k=0}^{N-1} f(j,k) \exp\left(-2\pi i\left(\frac{uj}{M} + \frac{vk}{N}\right)\right) \quad (1)$$

u,v are the number of row and column in the frequency domain; j,k are the number of row and column in the spatial domain; $F(u,v)$ is the image value in the frequency domain; $f(j,k)$ is the image value in the spatial domain; and i is the imaginary unit, $i = \sqrt{-1}$.

The result of a two dimensional DFT is a complex quantity. It can be displayed using the real as well as the imaginary part or the magnitude and phase. In this study, we use both the real and the imaginary parts as conditioning information in the groundwater model calibration process.

Characterization of pattern by discrete wavelet transformation (DWT)

The wavelet transformation is a further development of the fourier transformation. It overcomes the big disadvantage of the fourier transformation, which only has frequency resolution but no time resolution in signal processing. In image processing, the wavelet transformation is used frequently for image restoration, image compression and image denoising (Froment and Mallat, 1992; DeVore et al., 1992; Said and Pearlman, 1996). The mathematical form of the continuous wavelet transform for a one dimensional signal $f(x) \in L^2(R)$ is given by Eq. (2) (Grossmann and Morlet, 1984).

$$W(a,b) = \frac{1}{\sqrt{a}} \int_{-\infty}^{+\infty} f(x) \Psi^*\left(\frac{x-a}{b}\right) dx \quad (2)$$

a is the scale parameter (>0); b is the position parameter; and Ψ^* is the wavelet.

There are many types of wavelets commonly used in the DWT e.g. Daubechies wavelets, Biorthogonal wavelets etc. (Addison, 2002). In this study, we select the Biorthogonal wavelets (Lennon, 2005) and use the image compression function of the DWT.

The DWT is defined by a square matrix of filter coefficients, transforming an array into a new array, usually of the same dimension. The transformation is chosen in a way to achieve the highest possible reduction of data (also referred to image compression). This implies that high frequencies of the original image are excluded by the filter and the low frequencies, which represent the basic properties of the original image, are retained. By reconstructing the image after the DWT, we have a new image with a reduced resolution, depending on the DWT levels applied. Fig. 1 illustrates how the DWT works. In this example, the DWT is carried out at two levels (more levels are feasible as well). The advantage of DWT is that we can compare images based on coarser resolution without losing the basic characteristics of the original image.

Application

Study area

The project area, the Yanqi Basin, is located in the northwestern part of China (see Fig. 2). The climate is continental and dry. The mean annual precipitation is 50 mm (weather station at Korla). Compared to the mean annual potential evapotranspiration of 1400 mm, precipitation is negligible. Therefore agriculture is only feasible with full irrigation. The biggest river in the basin is the Kaidu River, which originates from the Tianshan Mountains in the northwest and flows into Bostan Lake in the southeast. Bostan Lake is the biggest fresh water body in the west of China. The outflow of Bostan Lake is the Kongque River which is the only exit

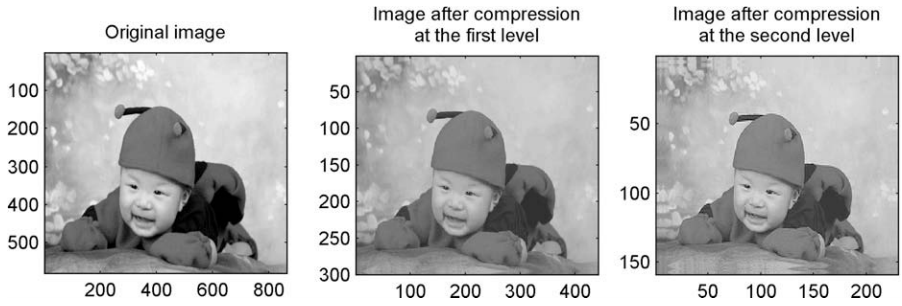

Fig. 1. Sketch of applying DWT to an image. The *x*-axis and *y*-axis in the three images represent the pixel coordinates in the matrix of each image. The matrix dimensions of the images are 581 × 865 (on the left hand side), 300 × 442 (in the middle) and 159 × 230 (on the right hand side).

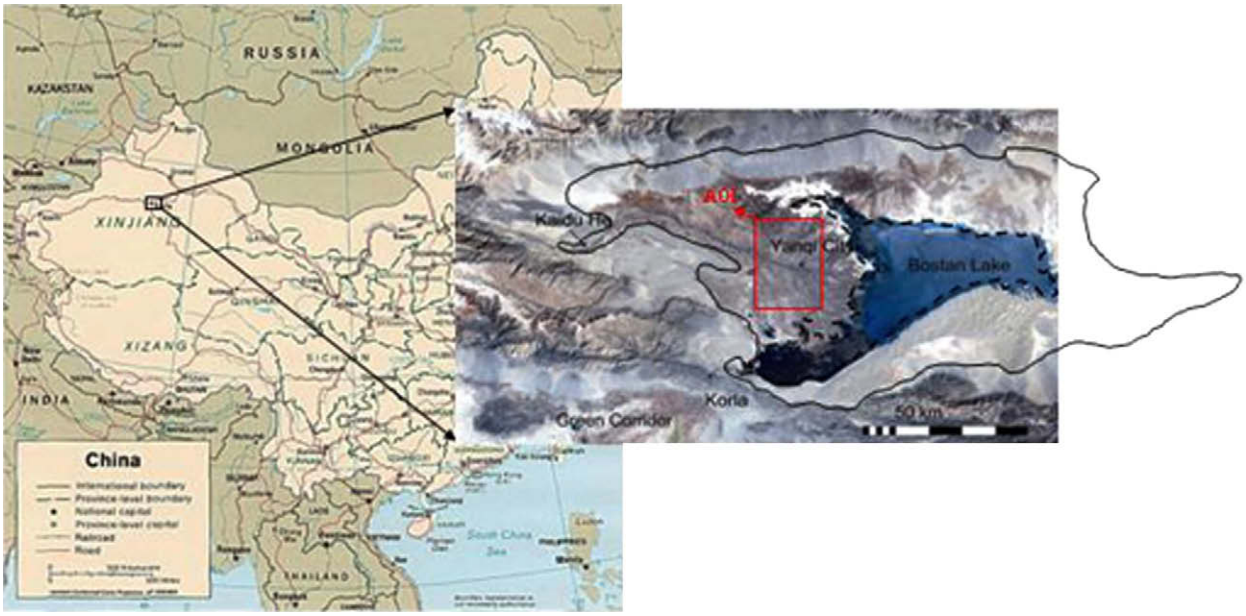

Fig. 2. Map of the Yanqi Basin.

of the entire basin. It connects the Yanqi Basin with the so-called Green Corridor in its downstream.

The agricultural activities in the Yanqi Basin started in the 1950s with flood irrigation techniques. The groundwater table has been raised since then, as a consequence of the inefficient irrigation practices and the absence of an effective drainage system. According to the field data obtained in 2000 (Dong et al. 2001), the depth to groundwater in the irrigated regions of the basin is in generally between 0.5 m and 3 m. As a result of the shallow groundwater table and high evaporation, soil salinization has become one of the most serious environmental problems in this region.

From the hydrological monitoring data of 1990–1999, the average annual water balance of the Yanqi Basin is shown in Fig. 3.

Groundwater model settings

A groundwater model has been established using MODFLOW 2000 (Harbaugh et al., 2000). The model area is marked by the solid black line and the lake area is marked by the dashed black line in the right hand side map of Fig. 2. The model is discretized horizontally with a cell resolution of 500 m × 500 m and a matrix of 169 rows × 370 columns × 4 layers. The boundaries are presented in Fig. 4. The closed shape of the Yanqi Basin as well as the sharp borders between different geological compartments makes the definition of the boundaries and zones straightforward. All outside boundaries of the modeling area being the physical limit of the aquifer are set as impermeable. The boundary conditions (except for Bostan Lake) are set equally for all layers. The first model layer is defined as a layer convertible between confined and unconfined state. All other layers are confined. A digital terrain model was constructed using radar images. The DEM was verified by D-GPS measurements on the ground at 60 locations. The average accuracy in the area of interest (AOI) is around 1.7 m. A detailed description of the construction and verification of the DEM is given by Brunner (2005). The aquifer properties such as hydraulic conductivity are defined by zonation on the basis of geological maps. The zonation of the horizontal hydraulic conductivity of the first layer is displayed in Fig. 4. The zonation of the horizontal hydraulic conductivity of the deeper layers is similar, except that the yellow zone, orange zone, and the lake zone are merged into one zone. The vertical hydraulic conductivities have the same zonation as the horizontal hydraulic conductivities of the deeper layers except for merging the green and magenta zones into one zone.

Recharge originates mainly from agricultural irrigation and was calculated by reducing the amount of irrigation water applied by the transpiration of vegetation and the direct evaporation of irrigation water during flood irrigation. The amount of irrigation water applied has been documented on a monthly basis for the period 1990–2000. The transpiration rates were calculated on a monthly

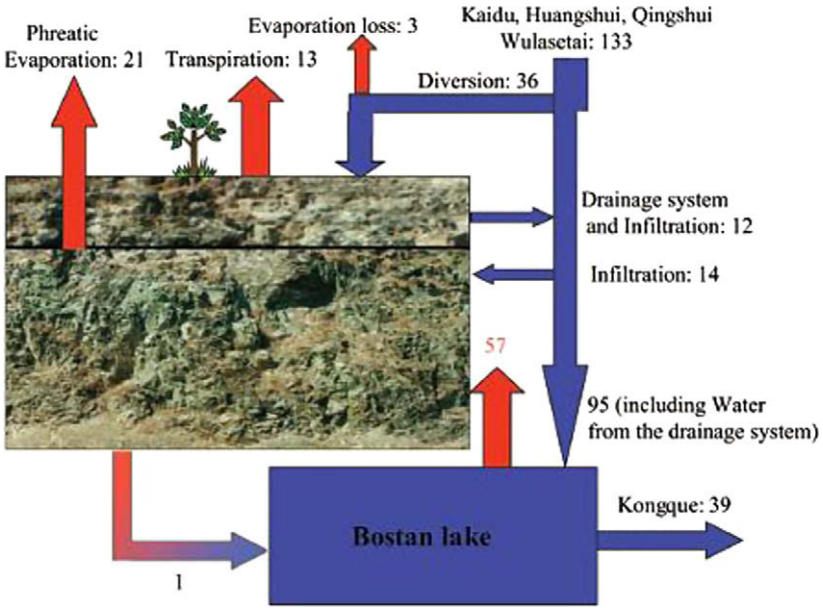

Fig. 3. Average water balance for the period 1990–1999 (m^3/s).

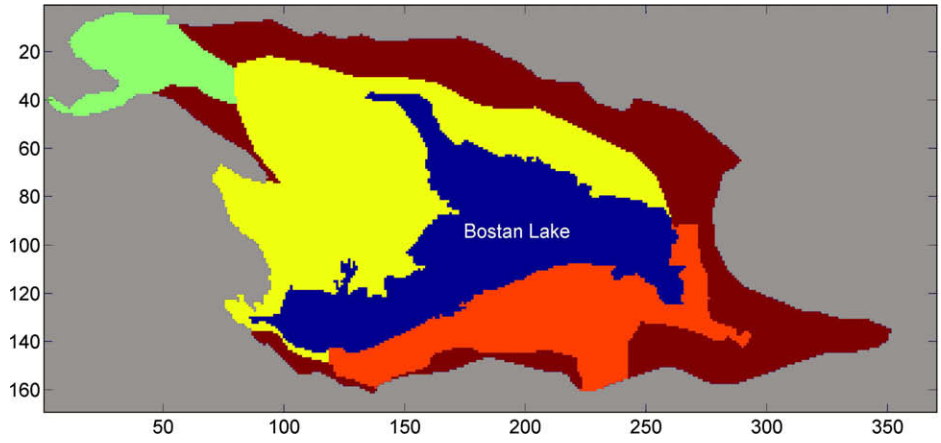

Fig. 4. Zonation of horizontal hydraulic conductivity of the first layer. The part in blue is the lake area. The part in grey is the area with inactive cells. The coordinates are given in the grid dimension. 1 grid cell = 500 m × 500 m. (For interpretation of the references to colour in this figure legend, the reader is referred to the web version of this article.)

basis using potential evaporation and the crop mix following guidelines of the FAO (Allen et al., 1998). Due to the relatively homogeneous distribution of irrigation channels up to the 4th order, the irrigation channels are not simulated directly in the model. Their infiltration is added to the groundwater recharge under the irrigated fields, the location of which is congruent with the location of the smallest irrigation channels (see Brunner, 2005). The networks of the river system and the drainage system as well as the lake boundary are illustrated in Fig. 5. The river system and the drainage system are both simulated by the Stream-Flow Routine package (SFR; Prudic et al., 2004; Niswonger and Prudic, 2005). Bostan Lake is simulated by the lake package (LAK; Merritt and Konikow, 2000).

Evaporation is simulated by the ETS package for Modflow (Banta, 2000) which uses the linear segment evaporation function. A minor modification has been made to the evaporation package to take the sub-cell elevation information into account which can improve the accuracy of evaporation simulation as illustrated by Li et al. (2008). As there are measured evaporation rates from stable isotope profiles, one could think that the evaporation curve is known (Brunner et al., 2008). However, values could only be obtained between depths of 0.85 m and 2 m. Following Brunner et al. (2008) and Hu et al. (2003), we use an evaporation function which is illustrated in Fig. 6. The maximum evaporation rate is 0.875 m/a and the extinction depth is set to 6.5 m. According to an unpublished report by the Xinjiang Agricultural University (2005) the extinction depth in the Yanqi basin can be as large as 6.5 m. This estimate is consistent with a modeling approach carried out by Shah et al. (2007). They estimated the extinction depth for different soil types and land covers. For clay and silty clay covered with grass the extinction depth is between 5.5 m and 7.15 m.

Evaporation map derived from the remote sensing data

The Advanced Very High Resolution Radiometer (NOAA-AVHRR) data with a resolution of 1 km have been selected and interpreted with a soil energy balance to obtain a spatially distributed ET estimate. As illustrated by Brunner et al. (2008), the ET map can be split into an evaporation map and a transpiration map by combining ET estimates based on NOAA images with

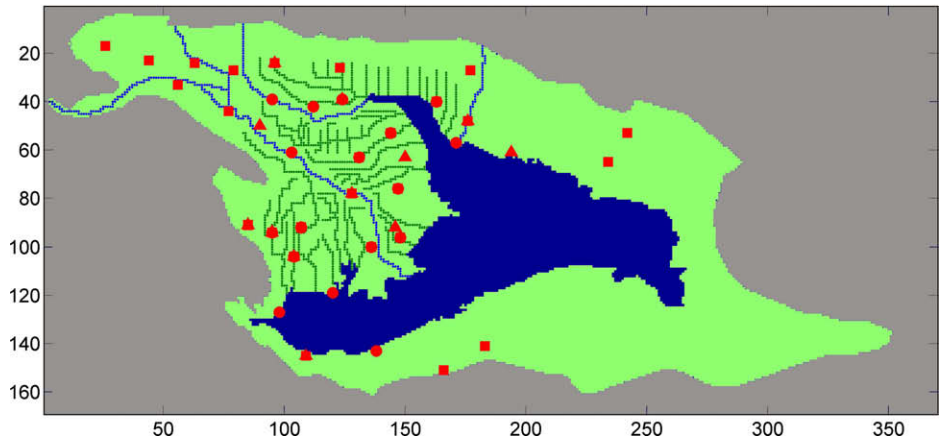

Fig. 5. Networks of the river system (in blue) and drainage system (in dark green) and boundary of Bostan Lake in the first layer of the groundwater model. The grey part is the area with inactive cells. The coordinates are given in the grid dimension. 1 Grid cell = 500 m × 500 m. The points in red are head observation wells. Square symbols represent observations in the first layer, circles observations in the second layer and triangles observations in the third layer. (For interpretation of the references to colour in this figure legend, the reader is referred to the web version of this article.)

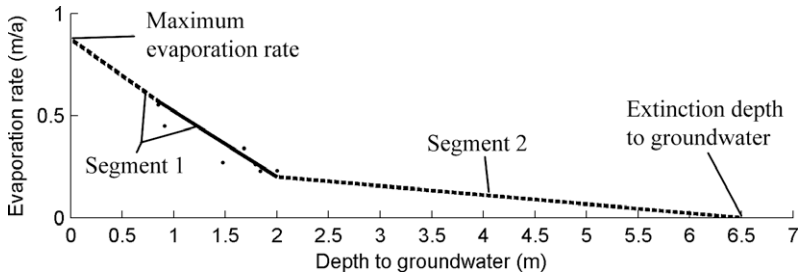

Fig. 6. Map of the linear segment evaporation function. Segment 1 is the combination of the regression line (solid line) from the stable isotope profiles which were only determined between 0.85 m and 2 m (at seven locations) and its extension to the y-axis (dashed line on the left hand side of the solid line). Segment 2 is the linear connection between the last point of Segment 1 and the extinction depth (dashed line on the right hand side of the solid line).

point-wise in situ measurements of phreatic evaporation by stable isotope measurements. In the model calibration process, the evaporation map is used as conditioning information.

Automatic model calibration settings

Conditioning information

In the calibration process, 55 head data (see Fig. 5) and the evaporation pattern obtained from NOAA images are taken as conditioning information. To facilitate the mathematical transformation of the pattern into frequency domain, a rectangular area of interest (AOI) has been selected which is illustrated by the red rectangle shown in Fig. 2. In the AOI, the distance from the top surface to the groundwater table is in general between 0.5 m and 2.5 m, i.e. in the range within which evaporation occurs. The selected area is also the core area of agricultural activities in the model area. In the model calibration process, only the evaporation patterns in the AOI both from the evaporation map derived from RS images and from the groundwater model are compared. In order to compare the evaporation patterns from two different sources on the same scale, the simulated evaporation with the resolution of 500 m × 500 m from the groundwater model is summed up for the corresponding NOAA image pixels which have a resolution of about 1 km.

Adjustable parameters

In this study, five parameters are selected as adjustable parameters. This choice has been made on the basis of a sensitivity study. Only highly sensitive parameters are adjusted. The horizontal and vertical hydraulic conductivities of the first and second layers are of great importance in simulating the spatial distribution of evaporation correctly since they are the dominant factors which can influence the flow field. The hydraulic conductivity of the streambed plays a critical role in simulating the groundwater heads along the rivers and drainages. For the less sensitive parameters best estimates from field data are used. All the adjustable parameters in PEST are set as relative values (see Table 1).

Calibration cases

We carry out several calibration runs using different combinations of the head data and the characterisations of the evaporation pattern. In the first case we consider only head data from the available boreholes. In a second step, we include the patterns of phreatic evaporation and test the different image transformations. Finally, we calibrate the model using the pattern information only. The seven different combinations are shown in Table 2.

Calibration process

The calibration process is illustrated in Fig. 7. The objective function is composed of two parts, one describing the squared difference between the observed and computed head vector and the other one the squared difference between observed and computed evaporation pattern. In Fig. 7, E represents the evaporation pattern in spatial or frequency domain. Since we have two different types of observation data (head data and evaporation pattern data), weighting factors for each type of observation data are needed. As shown in Fig. 7, ω_H and ω_E are the weighting factors (ω_H for

Table 1
Overview of adjustable parameters.

Parameter name	Description
hk1_factor	Ratio of the horizontal hydraulic conductivity to the initial horizontal hydraulic conductivity in the yellow zone of the first layer (Fig. 4) (initial value = 0.9 m/d)
hk2_factor	Ratio of the horizontal hydraulic conductivity to the initial horizontal hydraulic conductivity in the zone of the second layer which is merged by the yellow and orange zones and the lake zone (Fig. 4) (initial value = 15 m/d)
vk_factor	Ratio of the vertical hydraulic conductivity to the initial vertical conductivity in the zone of all the four layers which is merged by the yellow and orange zones and the lake zone (Fig. 4) (for first layer, the lake cells are excluded). (initial value = 0.09 m/d)
rc_factor	Ratio of the hydraulic conductivity of the streambed to the initial hydraulic conductivity of the streambed of all the rivers
dc_factor	Ratio of the hydraulic conductivity of the streambed to the initial hydraulic conductivity of the streambed of all drainages

Table 2
Overview over the different calibration cases.

Calibration case	Conditioning information			
	Heads	Evaporation pattern		
		Char.1	Char. 2	Char. 3
Case1	Yes	No	No	No
Case2	Yes	Yes	No	No
Case3	Yes	No	Yes	No
Case4	Yes	No	No	Yes
Case5	No	Yes	No	No
Case6	No	No	Yes	No
Case7	No	No	No	Yes

Char1: Characterization of pattern by relative values in the spatial domain.
Char2: Characterization of pattern by discrete fourier transformation (DFT).
Char3: Characterization of pattern by discrete wavelet transformation (DWT).

the head term and ω_E for the evaporation pattern term). The settings of weighting factors for all the calibration cases are as follows:

- Calibration only with head data: $\omega_H = 1$, $\omega_E = 0$.
- Calibration only with the evaporation pattern: $\omega_H = 0$, $\omega_E = 1$.
- Calibration with head data and evaporation pattern: $\omega_H = 1/$(variance of observed heads), $\omega_E = 1/$(variance of evaporation pattern from RS).

The automatic calibration tool PEST (Doherty, 2005) which is a nonlinear and model-independent parameter estimation software, was used in the calibration process. It uses the least-squares method (Marquardt, 1963; Levenberg, 1944). The mathematical transformations were carried out by using the functionalities of MATLAB.

Calibration results

Comparison of heads

Fig. 8 shows the head comparison after calibration for all the cases.

For all calibration cases, the simulated hydraulic heads fit the measured hydraulic heads very well (correlation coefficient $R = 0.99$ in all cases). From the head comparison of Cases 5–7, we see that the heads can be reproduced even without head data as conditioning information. Although the correlation coefficients between the observed heads and simulated heads of all the calibration cases are 0.99, the head objective function values (sum of difference squares) in each case are different (see Table 3). Case 1 shows the best fit of heads since only the head data are used in the calibration procedure. For the other cases, the head terms of

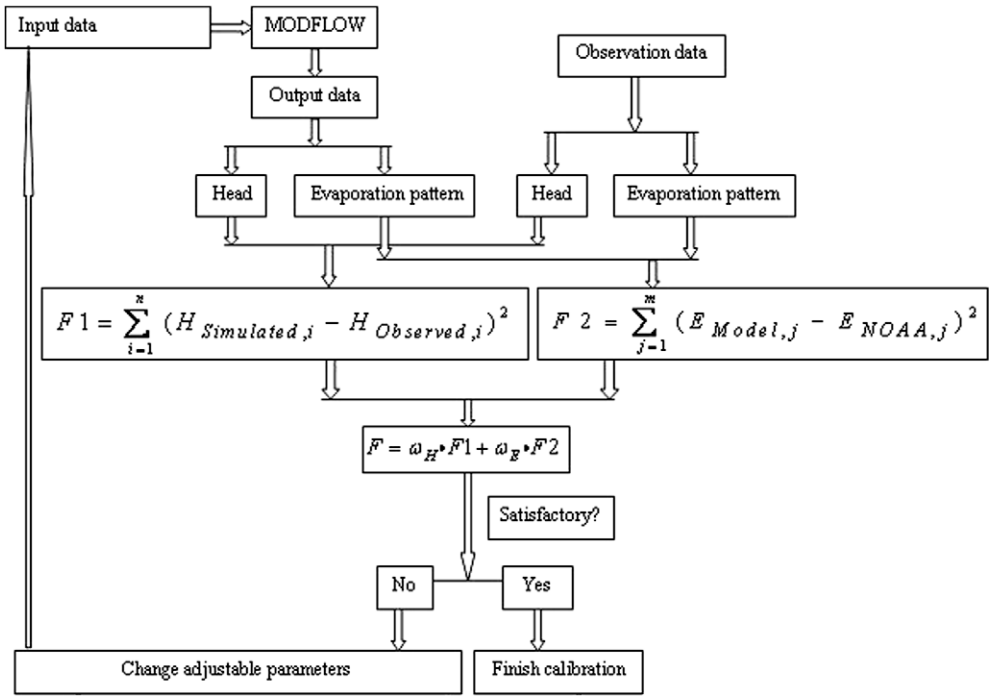

Fig. 7. Scheme of the calibration process. E means the evaporation pattern in spatial or frequency domain. ω_H and ω_E are the weighting factors of the head term and the evaporation pattern term. Calibration only with head data: $\omega_H = 1$, $\omega_E = 0$; Calibration only with the evaporation pattern: $\omega_H = 0$, $\omega_E = 1$; Calibration with head data and evaporation pattern: $\omega_H = 1/$(variance of observed heads), $\omega_E = 1/$(variance of evaporation pattern from RS).

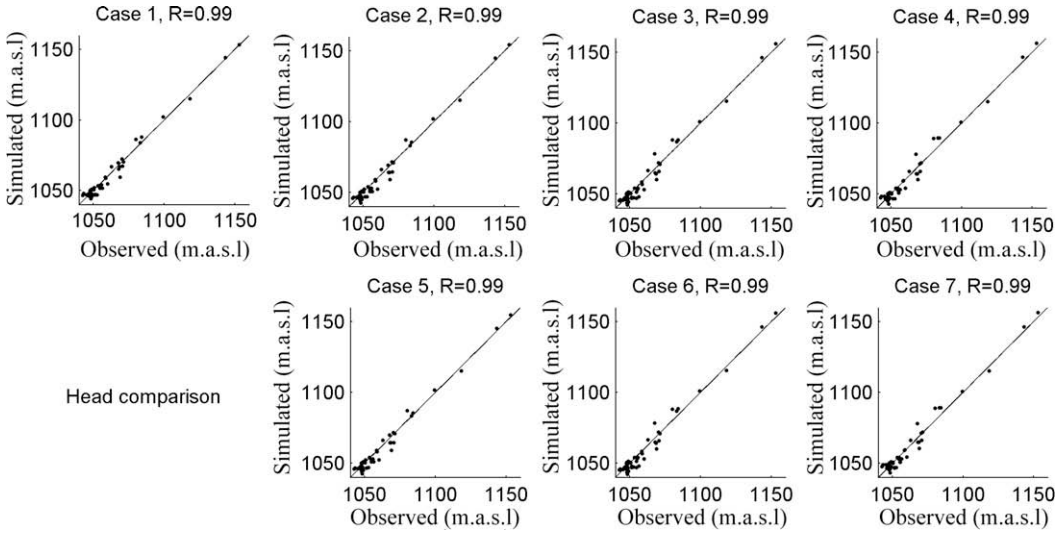

Fig. 8. Comparison of simulated and measured hydraulic heads for all calibration cases. *R* is the correlation coefficient.

Table 3
Table of summed difference squares of heads for all calibration cases (weighted).

Case 1	Case 2	Case 3	Case 4	Case 5	Case 6	Case 7
0.93	1.19	1.56	1.55	1.18	1.56	1.49

the objective function increase. However, they are still acceptable as we can see from Fig. 8.

Comparison of evaporation patterns (relative values)

The evaporation pattern has been characterized in three different ways in this study. However, all originate from the relative values in space domain. The relative pattern in space domain is therefore chosen for a comparison of the computed and measured patterns. Fig. 9 shows the comparison between the measured relative evaporation pattern and the relative values computed in all the calibration cases.

Obviously, the goodness-of-fit between the evaporation patterns from NOAA images and the groundwater model is much better if we take the evaporation pattern into account as conditioning information in the model calibration process, independent of the way how the evaporation pattern is characterized. If we look at Fig. 9 along columns, comparing Case 2 vs Case 5, Case 3 vs Case 6, and Case 4 vs Case 7, we can see that the head data do not help significantly in the model calibration process. The objective functions of the evaporation pattern term of each case are shown in Table 4. Table 5 shows the total evaporation in all cases.

Table 4
Table of summed difference squares of relative values from evaporation pattern (weighted).

Case 1	Case 2	Case 3	Case 4	Case 5	Case 6	Case 7
979.30	534.17	578.68	667.71	534.17	578.68	667.71

Table 5
Table of evaporation over the entire model domain (m^3/s).

Case 1	Case 2	Case 3	Case 4	Case 5	Case 6	Case 7
21.3	21.3	22.6	25.5	21.3	22.6	25.7

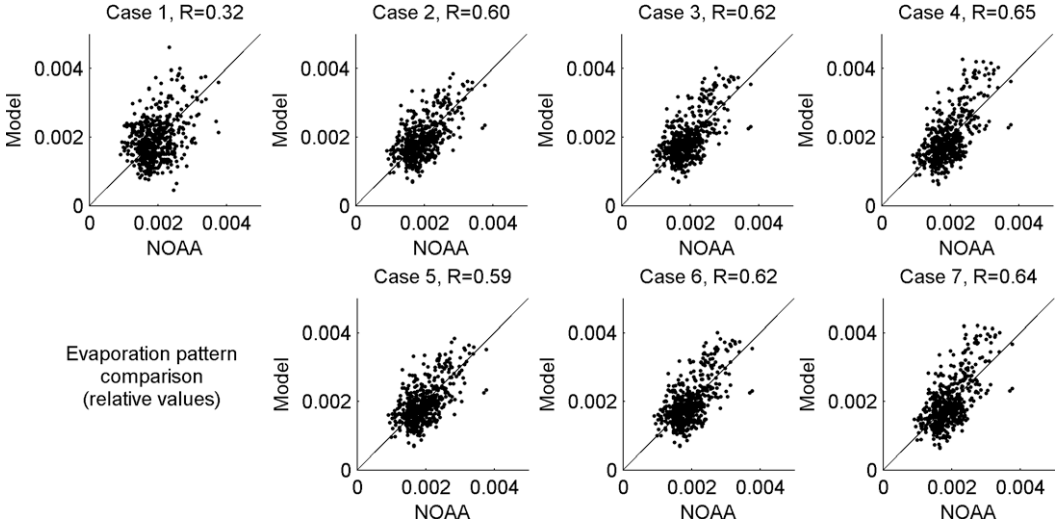

Fig. 9. Comparison of remotely sensed and simulated evaporation pattern (relative values). *R* is the correlation coefficient.

Table 6
Table of optimized values of the adjustable parameters.

Optimized parameters	Case 1	Case 2	Case 3	Case 4	Case 5	Case 6	Case 7
hk1_factor	0.10	29.95	27.83	30.00	28.48	27.47	22.50
hk2_factor	1.02	0.35	0.34	0.37	0.40	0.36	0.46
vk_factor	0.03	0.03	0.01	10.00	0.04	0.01	9.90
rc_factor	0.67	0.89	3.47	6.30	0.97	3.56	5.41
dc_factor	0.10	0.35	0.20	0.49	0.33	0.19	0.60

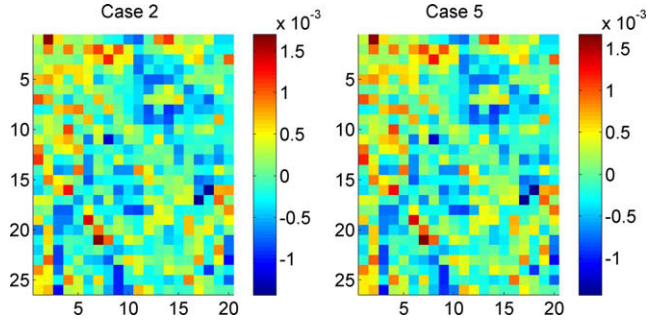

Fig. 10. Spatial distributions of difference between remotely sensed and simulated evaporation pattern (Case 2 and Case 5 in relative values).

Statistics of optimized parameters

The optimized values of the adjustable parameters are shown in Table 6.

From Table 6, we can see that we get quite different sets of adjustable parameters depending on whether we consider the evaporation information in the model calibration or not. With different characterizations of the evaporation pattern in the model calibration process, we also get some very differently optimized values, e.g. vk_factor in Case 5 and Case 7. The reason is that with different characterizations, the dominant cells which contribute more in the summed difference squares of heads and evaporation pattern data (objective function) are different. E.g. in Case 5, the objective function may be controlled by the cells with large values in the space domain. However, after the DFT transformation in Case 6, the cells with big values in space domain in Case 5 may have very low values in the frequency domain while the objective function in Case 6 may be controlled by the cells with higher frequencies. This difference results in the difference in the values of optimized parameters.

In the calibration cases which use the evaporation pattern as conditioning information (observed data), Case 2 and Case 5 define the evaporation pattern in the spatial domain; Case 3, Case 4, Case 6 and Case 7 define the evaporation pattern in the frequency domain. From the optimized values of the adjustable parameter and the objective functions of heads and evaporation patterns alone, it is hard to decide which case is the best. The correlation

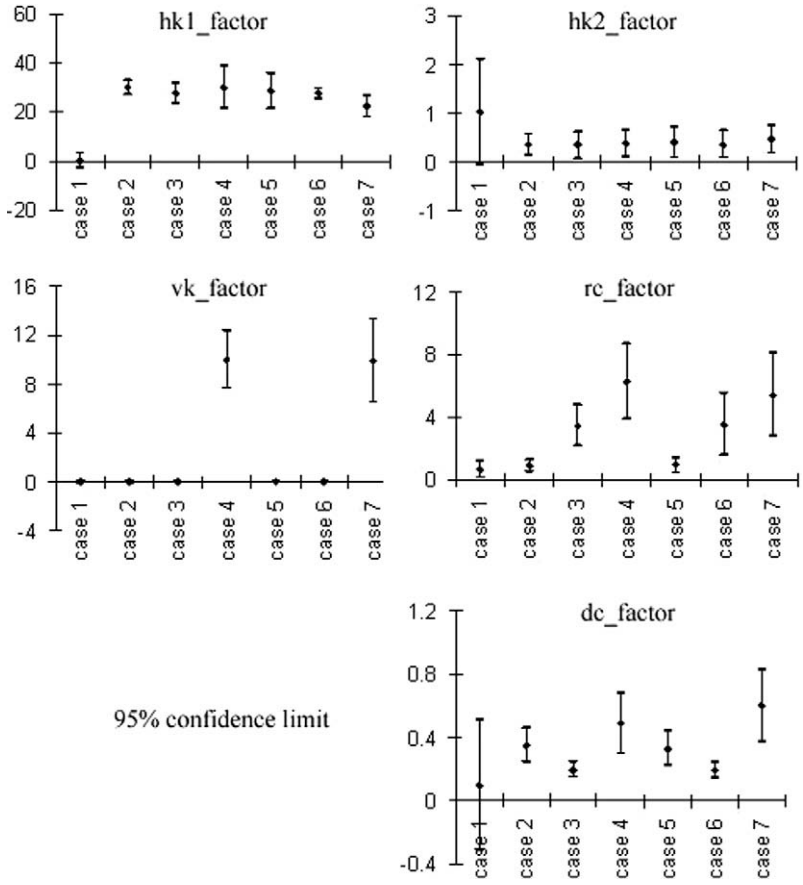

Fig. 11. 95% Confidence limit of the adjustable parameters. The dot is the optimized value (also see Table 6). The line shows the upper and lower confidence limits.

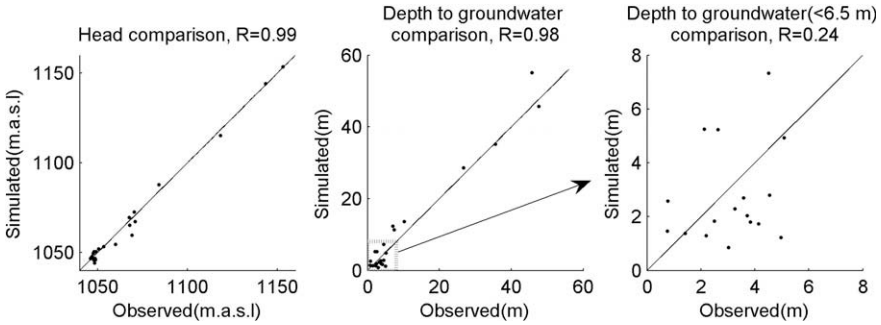

Fig. 12. Comparison of measured and computed heads and measured and computed depths to groundwater. All observation points are located in the first layer of the groundwater model.

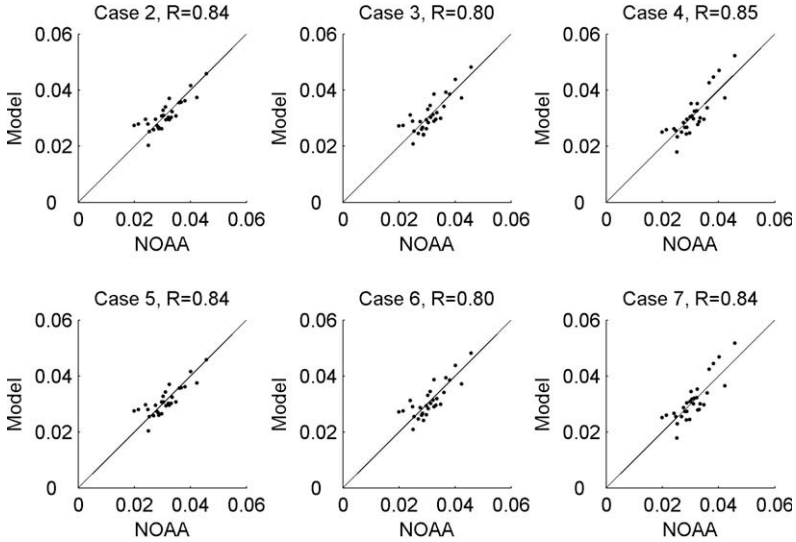

Fig. 13. Comparison of evaporation pattern (relative values) on a scale of 4 km. The value for a 4 km × 4 km cell is calculated by summing up the values in the corresponding 1 km × 1 km cell.

coefficients of all pairs of different adjustable parameters are less than 0.6 which means the identified parameters are more or less independent. However, if we look at the 95% confidence limit of the adjustable parameters after calibration, preferable cases can be identified. Fig. 11 shows the 95% confidence limit of the adjustable parameters in all the calibration cases.

From Fig. 11, we can see that the parameters obtained in Case 2 and Case 5 overall have less uncertainty than those from the other calibration cases. From Fig. 10 we see that these two cases also show the least spatial correlation of the difference between measured and computed patterns. The parameter values themselves are practically the same for both cases. From Table 5, we can see that in these two cases we get the total evaporation closest to the value shown in the water balance (Fig. 3). The latter is obtained directly from observation data of in- and outflows and the imposed irrigation flux.

Conclusions and discussions

From the head comparison (Fig. 8), we can conclude that a good fit of observed and simulated hydraulic heads can be obtained through the model calibration even if only the evaporation pattern is used as conditioning information. This result is independent of the characterization of the evaporation pattern. The evaporation pattern can replace the role of the hydraulic head data in the model calibration process at least in the model region where depth to groundwater is smaller than the extinction depth. From the evaporation pattern comparison (Figs. 9 and 10), we can see that the head data hardly influence the model calibration process if the evaporation pattern is considered. As a result from the comparisons of heads and evaporation patterns, the head data are practically dispensable in the model calibration process if we have the evaporation pattern information. The deeper reason for this is the fact that the evaporation law (Fig. 6) establishes a relation between evaporation and depth to groundwater, i.e. heads. So evaporation information – even if it is only a relative pattern – contains head information.

From all the cases with different characterizations of evaporation pattern (Cases 2–7), we can see that it is very hard to get a good fit of evaporation patterns from the NOAA images and the groundwater model although the heads can be fitted well as shown in Figs. 8 and 9. The correlation of measured and simulated heads looks so good because we compare the whole region which shows a maximum head difference of about 100 m. However, if we compare the depths to groundwater in those observation points where the depth to groundwater is shallow, the correlation becomes poor (see Fig. 12, simulated heads are from the first layer of Case 1). Actually, evaporation only occurs in the cells with a shallow depth to groundwater (above the extinction depth to groundwater, which is 6.5 m in this study). On the other hand, the depth to groundwater is one of the dominant variables in the calculation of evaporation. The scatter of the evaporation pattern corresponds to the scatter of the depth to groundwater if we recall the linear segment evaporation function shown in Fig. 6.

There are two main reasons to explain the scatter of the evaporation pattern. On one hand, the evaporation pattern based on the remote sensing images is associated with uncertainty both from the images and the interpretation method used. Although we avoid using the absolute values of evaporation, uncertainties cannot be eliminated completely. More details about the uncertainties in calculating ET from remote sensing images and splitting ET into evaporation and transpiration are given in Brunner et al. (2008). On the other hand, the digital elevation model (DEM), which is another dominant component in the calculation of evaporation, is not accurate enough. As demonstrated by Li et al. (2008), the sub-cell variation of ground elevation is of relevance down to a level not resolved by the available DEM. In addition the available DEM introduces error. In this study, the DEM from the SRTM model (Rabus et al., 2003) was used. As stated by Brunner (2005), the average accuracy of the SRTM DEM in the AOI is around 1.7 m. In this study, after calibration with the evaporation pattern (Cases 2–7), the average error of depth to groundwater is also around 2 m which is comparable to the average accuracy of the DEM. We conclude that the inaccuracy of the DEM is the dominant uncertainty.

Still, the use of evaporation data brings considerable improvement. Cases 2–7 all show a smaller scatter of computed vs measured evaporation patterns than Case 1. As we have a large number of data points – compared to the limited number of head measurements – when comparing the evaporation patterns, we can filter the results by averaging them to a coarser scale. These findings are consistent with Immerzeel and Droogers, 2007 and Li et al. (2008). Fig. 13 shows the evaporation pattern comparison on a scale of 4 km for Cases 2–7.

Further information on the quality of results obtained with different methods can be abstracted from the difference pattern (Fig. 10) and the total absolute evaporation computed (Table 5). Here Case 2 and Case 5 show the least spatial correlation of error and the best water balance closure.

The main idea in this study was to introduce the spatial evaporation pattern as conditioning information in the groundwater model calibration. It shows that the use of evaporation pattern information in the model calibration process can reduce the limitations of a small number of hydraulic head data available for model calibration. Although for both the head calibration and the pattern calibration the accuracy of the DEM is in principle insufficient, the spatially exhaustive information in the evaporation pattern allows filtering of the DEM errors. The comparison of evaporation patterns on a coarser scale shows that the errors in the DEM are unbiased and can be averaged away. The calibration on the basis of the pattern is more trustworthy than the calibration on the basis of a few local heads or depths to groundwater.

Acknowledgments

We thank Dr. Harrie-Jan Hendricks Franssen at IfU for generous help. We also thank the three anonymous reviewers. Their comments helped to significantly improve this manuscript.

References

Addison, P.S., 2002. The Illustrated Wavelet Transform Handbook. Institute of Physics Publishing. 65–141.

Allen, R., Pereira, L., Raes, D., Smith, M., 1998. Crop Evapotranspiration-Guidelines for Computing Crop Water Requirements. FAO Irrigation and Drainage Paper No. 56. FAO, Rome.

Anon., 1990. Use of Remote Sensing for Hydrogeological Studies in Humid Tropical areas. A pilot study in West Java, Indonesia. IWACO/TNO/ÎTC. Min. Public Works, Indonesia.

Arnold, J.G., Srinivasan, P., Muttiah, R.S., Williams, J.R., 1998. Large area hydrologic modeling and assessment. Part I. Model development. Journal of the American Water Resources Association 34, 73–89.

Banta, E.R., 2000. MODFLOW-2000, the U.S. Geological Survey Modular Ground-Water Model – Documentation of Packages for Simulating Evapotranspiration with a Segmented Function (ETS1) and Drains with Return Flow (DRT1). U.S. Geological Survey Open-File Report 00-466, 127 p.

Bastiaanssen, W., Menenti, M., et al., 1998a. A remote sensing surface energy balance algorithm for land (SEBAL) – 1. Formulation. Journal of Hydrology 213, 198–212.

Bastiaanssen, W.G.M., Pelgrum, H., et al., 1998b. A remote sensing surface energy balance algorithm for land (SEBAL) – 2. Validation. Journal of Hydrology 213, 213–229.

Bauer, P., Held, R., Zimmermann, S., Linn, F., Kinzelbach, W., 2006. Coupled flow and salinity transport modeling in semi-arid environments: the Shashe River Valley, Botswana. Journal of Hydrology 316 (1–4), 163–183.

Bobba, A.G., Bukata, R.P., Jerome, J.H., 1992. Digitally processed satellite data as a tool in detecting potential groundwater flow systems. Journal of Hydrology 131, 25–62.

Brunner, P., 2005. Water and salt management in the Yanqi Basin, China, Ph.D. Diss, ETH Zurich No.16210, ISBN 3-906445-26-7. <http://e-collection.ethbib.ethz.ch/show?type=diss&nv=16210>.

Brunner, P., Bauer, P., Eugster, M., Kinzelbach, W., 2004. Using remote sensing to regionalize local precipitation recharge rates obtained from the Chloride Method. Journal of Hydrology 294, 241–250.

Brunner, P., Hendricks Franssen, H.J., Kgotlhang, L., Bauer-Gottwein, P., Kinzelbach, W., 2007. How can remote sensing contribute in groundwater modeling? Hydrogeology Journal 15 (1), 5–18.

Brunner, P., Li, H.T., Kinzelbach, W., Dong, X.G., 2008. Extracting phreatic evaporation from remotely sensed maps of evapotranspiration. Water Resources Research 44, W08428. doi:10.1029/2007WR006063.

Choudhury, B.J., 1994. Synergism of multispectral satellite observations for estimating regional land surface evaporation. Remote Sensing of Environment 49, 264–274.

DeVore, R.A., Jawerth, B., Lucier, B.J., 1992. Image compression through wavelet transform coding. IEEE Transaction on Information Theory 38 (2), 719–746.

Doherty, J., 2005. PEST: Model-Independent Parameter Estimation, User Manual. fifth ed.. Watermark Computing, Brisbane.

Dong, X.G., 2005. Monitoring of Water and Salt and Groundwater Model Application in the Yanqi Basin. Xinjiang Agricultural University.

Dong, X., Jiang, T., Jiang, H., 2001. Study on the pattern of water resources utilization and environmental conservation of Yanqi Basin. In: Li, G. (Ed.), Development, Planning and Management of Surface and Groundwater Resources. IAHR Congress Proceedings. Tsinghua University Press, Beijing, China, pp. 333–340.

Du, W.C., Ye, D.L., 1993. Methods for recognizing and extracting groundwater information from remote sensing data. Proc. Int. Symp. Operationalization of Remote Sens, vol. 9. Earth Science Applications, ITC, Enschede, The Netherlands, pp. 105–111.

El Hadanai, D., Limam, N., El Meslouhi, R., 1993. Remote sensing applications to groundwater resources. Proc. Int. Symp. Operationalization of Remote Sens, vol. 9. Earth Science Applications, ITC, Enschede, The Netherlands, pp. 93–103.

Hendricks Franssen, H.J., Brunner, P., Makobo, P., Kinzelbach, W., 2008. Equally likely inverse solutions to a groundwater flow problem including pattern information from remote sensing images. Water Resources Research 44, W01419. doi:10.1029/2007WR006097.

Froment, J., Mallat, S., 1992. Second generation compact image coding with wavelets. In: Chui, C.K. (Ed.), Wavelets: A Tutorial in Theory and Applications, vol. 2. Academic Press, NY.

Grossmann, A., Morlet, J., 1984. Decomposition of Hardy functions into square integrable wavelets of constant shape. SIAM Journal on Mathematical Analysis 15, 723–736.

Gupta, V.K., Sorooshian, S., Yapo, P.O., 1998. Towards improved calibration of hydrologic model: multiple and noncommensurable measures of information. Water Resources Research 34, 751–763.

Hall, F.G., Huemmrich, K.F., Goetz, S.J., Sellers, P.J., Nickelson, J.E., 1992. Satellite remote sensing of surface energy balance: success, failures, and unresolved issues in FIFE. Journal of Geophysical Research 97 (D17), 19061–19089.

Harbaugh, A. W., Banta, E.R., Hill, M.C., McDonald, M.G., 2000. MODFLOW-2000, the U.S. Geological Survey modular ground-water model – User guide to modularization concepts and the Ground-Water Flow Process. U.S. Geological Survey Open-File Report 00-92, 121 p.

Hu, S., Kang, S., Song, Y., Ceng, X., 2003. Calculating phreaitc water evaporation from bare soil for the Tarim River Basin, Xinjiang. In: Kang, S., Davis, B., Shan, L., Cai, H. (Eds.), International Conference on Water–Saving Agriculture and Sustainable Use of Water and Land Resources in Arid and Semi.-arid Areas. Shanxi Science and Technology Press, Yanglin, China, pp. 727–733.

Immerzeel, W.W., Droogers, P., 2007. Calibration of a distributed hydrological model based on satellite evapotranspiration. Journal of Hydrology 349, 411–424.

Kite, G.W., Droogers, P., 2000. Comparing evapotranspiration estimates from satellites, hydrological models and field data. Journal of Hydrology 229, 3–18.

Kite, G.W., Pietroniro, A., 1996. Remote sensing applications in hydrology. Hydrological Sciences 41, 563–592.

Lennon, D., 2005. (Bi) orthogonal Wavelets. <http://www.amath.washington.edu/~dnlennon/biorthogonal_wavelets.pdf>.

Levenberg, K., 1944. A method for the solution of certain non-linear problems in least squares. Quarterly of Applied Mathematics 2, 164–168.

Li, H.T., Kinzelbach, W., Brunner, P., Li, W.P., Dong, X.G., 2008. Topography representation methods for improving evaporation simulation in groundwater modeling. Journal of Hydrology 356, 199–208.

Maddock III, T., Baird, K.J., 2003. A riparian evapotranspiration package for MODFLOW-96 and MODFLOW-2000. HWR No. 02-03. Department of Hydrology and Water Resources, University of Arizona Research Laboratory for Riparian Studies, University of Arizona.

Marquardt, D.W., 1963. An algorithm for least-squares estimation of nonlinear parameters. Journal of the Society of Industrial and Applied Mathematics 11 (2), 431–441.

McDonald, M.G., Harbaugh, A.W., 1988. A modular three dimensional finite difference ground-water flow model. U.S. Geological Survey TWI 6-A1.

McDonald, M.G., Harbaugh, A.W., 1996. Programmer's documentation for MODFLOW-96, an update to the U.S. Geological Survey Modular Finite-difference Ground-Water Flow Model. U.S. Geological Survey, Open-File Report, 96–486.

Meijerink, A.M.J., 1996. Remote sensing applications to hydrology: groundwater. Hydrological Sciences Journal 41, 549–561.

Merritt, M.L., Konikow, L.F., 2000. Documentation of a Computer Program to Simulate Lake-Aquifer Interaction Using the MODFLOW Ground-Water Flow Model and the MOC3D Solute-Transport Model. U.S. Geological Survey Water-Resources Investigations Report 00-4167, 146.

Niswonger, R.G., Prudic, D.E., 2005. Documentation of the Streamflow-Routing (SFR2) Package to Include Unsaturated Flow Beneath Streams – A modification to SFR1. U.S. Geological Survey Techniques and Methods, Book 6, 47 p. (Chapter A13).

Poeter, E.P., Hill, M.C., 1997. Inverse models: a necessary next step in ground-water flow modeling. Groundwater Model 35, 250–260.

Pratt, W.K., 2001. Digital Image Processing: PIKS Inside, third ed. John Wiley & Sons, Inc. 189–236.

Prudic, D.E., Konikow, L.F., Banta, E.R., 2004. A New Stream-flow Routing (SFR1) Package to Simulate Stream-aquifer Interaction with MODFLOW-2000. U.S. Geological Survey Open-File Report 2004-1042, 95 p.

Rabus, B., Eineder, M., Roth, A., Bamler, R., 2003. The shuttle radar topography mission – a new class of digital elevation models acquired by spaceborne radar. Photogrammetry and Remote Sensing 57, 241–262.

Roerink, G.J., Su, Z., Menenti, M., 2000. S-SEBI: a simple remote sensing algorithm to estimate the surface energy balance. Physics and Chemistry of 17 the Earth Part B-Hydrology Oceans and Atmosphere 25 (2), 147–157.

Said, A., Pearlman, W.A., 1996. An image multiresolution representation for lossless and lossy image compression. IEEE Transactions on Image Processing 5 (9), 1303–1310.

Schmid, W., Hanson, R.T., Maddock III, T., Leake, S.A., 2006. User's guide for the Farm Process (FMP1) for the U.S. Geological Survey's Modular Three-Dimensional Finite Difference Ground-Water Flow Model, MODFLOW-2000. U.S. Geological Survey, Techniques and Methods Report 6-A17, 127p.

Shah, N., Nachabe, M., Ross, M., 2007. Extinction depth and evapotranspiration from ground water under selected land covers. Ground Water 45, 329–338.